Industrial Crops & Products 168 (2021) 113584

Contents lists available at ScienceDirect

Industrial Crops & Products

journal homepage: www.elsevier.com/locate/indcrop

Colloidal lignin nanoparticles from acid hydrotropic fractionation for producing tough, biodegradable, and UV blocking PVA nanocomposite

Huihui Wang [a,b], Xiaoyan Tang [b], Matthew A. Arvanitis [b], Vina Yang [b], Nicole Stark [b], Chuanfu Liu [a], John M. Considine [b], J.Y. Zhu [b,*]

[a] State Key Laboratory of Pulp and Paper Engineering, South China University of Technology, Guangzhou, China
[b] Forest Products Laboratory, U.S. Department of Agriculture Forest Service, Madison, 53726, USA

ARTICLE INFO

Keywords:
Lignin nanoparticles (LNPs)
Colloidal LNP
Composite film
Toughness
Biodegradability
UV blocking

ABSTRACT

Colloidal lignin nanoparticles (LNPs) from low temperature acid hydrotropic fractionation (AHF) of poplar wood and commercial alkali lignin using *p*-Toluenesulfonic acid (*p*-TsOH) were directly mixed with PVA to make PVA/AHF-LNP nanocomposite films. *p*-TsOH itself acted as a plasticizer for PVA; however the application of *p*-TsOH alone reduced PVA film tensile strength and therefore toughness. At proper loadings of LNPs and *p*-TsOH, both the failure strain and tensile strength of PVA/AHF-LNP composites were improved. The formation of hydrogen bonding between the *p*-TsOH/AHF-LNP aggregates with hydroxyl groups on PVA molecular chains, and the breakage and reforming of *p*-TsOH/AHF-LNP aggregates, along with the nanophase crazing due to the presence of *p*-TsOH/AHF-LNP aggregates were identified as the main mechanisms for improving the toughness of PVA/AHF-LNP nanocomposite. The composite also had improved UV shielding performance and biodegradability due to the presence of *p*-TsOH and LNPs compared with neat PVA. This nanocomposite film could be used as biodegradable anti-ultraviolet packing film.

1. Introduction

Nanoparticles can endow polymer nanocomposites with interesting functionalities, and therefore have been used in the formulations for industrial and consumer products (Ghosh et al., 2008; Luo et al., 2006; Morones et al., 2005; Salata, 2004). Lignin is one of the most abundant and underutilized biomaterials, and can be an excellent candidate in the synthesis of green nanoparticles (Ragauskas et al., 2014). Lignin nanoparticles (LNPs) possessed great potential for valorization because of their large surface area and rich surface functional groups (Lievonen et al., 2016; Tian et al., 2017). However, LNPs are currently not available commercially. Laboratory production of LNPs is not efficient, which often involves two steps (Zhu et al., 2021): (1) dissolving commercial technical lignin via chemical reactions (Cheng et al., 2012; Popa et al., 2011), or by means of solvents such as ethylene glycol (Frangville et al., 2012), acetone (Richter et al., 2016), tetrahydrofuran (THF) (Lievonen et al., 2016; Qian et al., 2014), or N,N-dimethylformamide (DMF) (Ago et al., 2016; Myint et al., 2016), and (2) precipitating the dissolved lignin in the form of nanoparticles chemically, e.g. using acids, (Frangville et al., 2012; Popa et al., 2011; Richter et al., 2016) or antisolvents (Lu et al., 2012; Myint et al., 2016), or physically through dialysis (Lievonen et al., 2016), atomization or drying (Ago et al., 2016). Although technical lignin is available commercially, the solvents used often cause environmental concerns.

Low temperature and atmospheric pressure acid hydrotropic fractionation (AHF) process can produce LNPs directly from raw lignocellulosic biomass (Bian et al., 2017; Chen et al., 2017; Ma et al., 2018). The process is scalable and eliminates the usage of organic solvents. The dissolved lignin in AHF can be precipitated simply by diluting the AHF spent liquor using water to below the minimal hydrotropic concentration (MHC). A fraction of AH-LNPs can be rather stable in the diluted spent liquor to become a stable colloidal AH-LNP suspension. Recent study indicated that colloidal nanoparticle system can be an enabling technology for a board applications (Lu et al., 2019). Therefore, utilizing the colloidal LNPs from AHF not only can address issues of recycle and reuse of spent liquor but also is a potential avenue for high value lignin valorization.

Improving composite toughness has great relevance to many practical applications. For example, cellulose nanofibril (CNF) films are brittle, which limits its commercial applications. A recent study showed

* Corresponding author.
E-mail address: junyong.zhu@usda.gov (J.Y. Zhu).

https://doi.org/10.1016/j.indcrop.2021.113584
Received 19 November 2020; Received in revised form 16 April 2021; Accepted 25 April 2021
Available online 7 May 2021
0926-6690/Published by Elsevier B.V.

Table 1
The compositions of the colloidal AH-LNP suspensions used for producing PVA/AH-LNP nanocomposites.

Sample[a]	Reaction conditions	LNP (wt %)	Xylose (g/L)	Glucose (g/L)	*p*-TsOH (g/L)
PW15−1.5	P15T80t60	0.036	0.12 ± 0	ND	15.5 ± 0.6
PW15−2.3	P15T80t60	0.072	0.16 ± 0.00	ND	22.4 ± 0.2
PW40−4.0	P40T80t60	0.018	0.56 ± 0.00	ND	38.0 ± 0.2
Alk15−1.5	P15T80t60	0.014	N/A	N/A	15.2
Alk15L	P15T80t60	0.237	N/A	N/A	152
Alk15H	P15T80t60	0.596	N/A	N/A	152

[a] PW stands for poplar wood lignin from flow-through AHF, the number after PW was *p*-TsOH concentration in wt% used in fractionation; Alk stands for batch dissolution of alkaline lignin using *p*-TsOH; The ending numbers after the dash were the *p*-TsOH concentration in wt% after dilution in the AH-LNP suspension (the last two samples were not diluted with L and H stand for low and high lignin loading of 0.3 and 1 g in 37.2 mL *p*-TsOH solution, respectively).

that incorporating colloidal LNPs into CNF films can improve CNF toughness, tensile strength, and UV protection capability (Farooq et al., 2018). The study suggested LNPs could act as a lubricating and stress transfer agent, which improved CNF film toughness and ductilibility. When bulk microsized lignin particles were incorporated into either CNF (Farooq et al., 2018) or PVA (Tian et al., 2017) films, no toughness improvement was observed. On the other hand, a recent study showed that adding lignosulfonate acid (LA) into a PVA system can form very strong and tough film via nanostructured microphase separation and intermolecular sacrificial hydrogen bond interactions (Zhang et al., 2019). *p*-TsOH in the AHF spent liquor as an acid hydrotrope has a hydrophobic end and a hydrophilic end to form a *p*-TsOH/LNP complex with colloidal AH-LPNs through hydrophobic interactions. Specifically, it was hypothesized that the lipophilic nonpolar part (toluene moiety) of the *p*-TsOH molecule can shield colloidal AH-LNPs through π-π stacking as well as hydrophobic interaction with LNP to form micellar-like aggregates to prevent the re-aggregation of lignin, whereas the hydrophilic end (sulfonic acid moiety) points outward to water for effective dissolution (Chen et al., 2017; Das and Paul, 2016). We can hypothesize that this colloidal *p*-TsOH/LNP complex system can play similar roles as LA to substantially enhance PVA film toughness and tensile strength based on the fact the main chemical structure in LA is lignin with a hydrophilic sulfonic acid end. The novelty of this work is to demonstrate that colloidal AH-LNPs in *p*-TsOH spent liquor can be an effective low-cost plasticizer for the manufacturing PVA/AH-LNP nanocomposite films, similar to LA (Zhang et al., 2019) with high toughness, biodegradability, and UV-blocking performance. The possible mechanistic interactions between AH-LNPs and the PVA matrix will also be studied. This work will add to the existing literature on using LPNs as a tool for developing tough, biodegradable, UV blocking lignin nanocomposites. Because preparing LA from lignosulfonate is quite tedious, while colloidal *p*-TsOH/LNP suspensions are readily available from AHF, the present study has significance for sustainable manufacturing.

2. Materials and methods

2.1. Materials

Poplar wood (Populus deltodes Barr. ex Marsh x p. nigra L) was harvested from Hugo Sauer Nursery in Rhinelander, WI, USA. The wood logs were manually debarked and chipped at the USDA Forest Products Laboratory, Madison, WI. The chips were hammer-milled into 20 mesh fiber bundles. *p*-TsOH of ACS regent grade was purchased from Sigma-Aldrich (St. Louis, MO, USA).

Two types of PVAs with molecular weight (Mw) of 89,000–98,000 (Product No. 341584) and 130,000 (Product No. 563900), respectively, were purchased from Sigma Aldrich (St. Louis, Mo). Alkali lignin (Product No. 370959) was used as received from Sigma Aldrich (St. Louis, MO, USA).

2.2. AHF of poplar wood

The hammer-milled poplar wood was fractionated according to the procedures described previously using a flow-through configuration (Wang et al., 2019b). Briefly, poplar wood of 3.7 g in oven dry weight was first loaded into a 20 mL polypropylene column. A fresh *p*-TsOH solution with the desired concentration was then flowed into the column at a flow rate of 0.62 mL/min for 60 min using a peristaltic pump. The resulting spent liquor was collected, diluted using deionized water (DI) water, and then centrifuged at 10,000 g for 10 min. After the centrifugation, the supernatant was further filtrated using a sand core funnel to completely remove the precipitant. The finally obtained supernatant was used as a colloidal AH-LNPs named PWxx-yy as listed in Table 1 with PW standing for poplar wood, xx representing the *p*-TsOH concentration in wt% used for fractionation, and yy representing the *p*-TsOH concentration in wt% after dilution.

2.3. Preparation of colloidal AH-LNPs using alkali lignin

Commercial alkali lignin described above was solubilized by *p*-TsOH to produce colloidal AH-LNPs. Batch runs were carried out by adding 0.3 g (low loading) or 1.0 g (high loading) of alkali lignin into aqueous *p*-TsOH of 37.2 mL at 15 wt% at 80 °C for 60 min. For the run using 0.3 g alkali lignin, part of the spent liquor was diluted to *p*-TsOH of 1.5 wt%. After centrifuging, the supernatant was collected and labelled as Alk15−1.5 (Table 1). The other part from the 0.3 g lignin loading run and the entire spent liquor from the run using 1.0 g lignin loading were filtrated using nylon membrane (pore size 0.45 μm, ChromTech) and then collected without dilution and labelled as Alk15 L and Alk15H, respectively (Table 1).

2.4. Preparation and recycling of PVA/AH-LNP nanocomposite films

The PVA/AH-LNP nanocomposite films were produced by solution casting (Tian et al., 2017). 1.25 g of PVA as received was added into 23.75 g of aqueous colloidal AH-LNP suspensions. For the two films produced using undiluted colloidal AH-LNP suspensions, approximately 1.0 and 1.5 g of Alk15 L and Alk15H, respectively, were added to approximately 24.0 g of aqueous PVA solution. The mixture was heated at 90 °C for 2 h with magnetic stirring. The resultant solution was sonicated for 10 min, degassed, then poured into a polytetrafluoroethylene (PTFE) dish, and air-dried at 50 °C overnight. Two sets of neat PVA films were also made using the two types of PVAs of different molecular weight with each film using 25.0 g PVA solutions of 5 wt%. The LNPs in different colloidal LNPs are not much significantly different. So, differentiation among LNP samples is not necessary and only for record.

The used PVA/AH-LNP nanocomposites were added into 25.0 g DI water. The mixture was heated at 90 °C for 2 h with magnetic stirring. The resultant solution was sonicated 10 min to degas, then poured into a PTEE dish, and air-dried at 50 °C overnight to produce film through solution casting. Recycling of PVA/AH-LNP nanocomposite was performed four times.

2.5. Chemical compositional analyses

The fractionated lignocellulosic solids were air-dried at 105 °C for 12 h, and ground to 20-mesh using a Wiley mill. The ground samples were hydrolyzed using sulfuric acid in two steps. The hydrolysate was analyzed for carbohydrate by the Analytical Chemistry and Microscopy Laboratory at the Forest Products Laboratory, as described previously (Luo et al., 2010).

2.6. Nuclear magnetic resonance (NMR) spectroscopic analyses

Chemical structures of whole cell wall (WCW) and colloidal AH-LNPs were analyzed by NMR. The WCW of poplar wood was ball-milled according to literature (Chen et al., 2017; Mansfield et al., 2012; Wang et al., 2019a). The ball-milled WCW was swollen in 0.5 mL of dimethyl sulfoxide (DMSO)-d_6-pyridine-d_5 (v/v 4:1). The LNPs in AHF spent liquor were dialyzed for two weeks. The resultant AH-LNPs were freeze-dried, and also dissolved in 0.5 mL of DMSO-d_6 for NMR analyses. 2D ^{13}C-^{1}H NMR analyses were performed on a Bruker (Billerica, MA) AVANCE III HD spectrometer at 27 °C. NMR data were analyzed with TopSpin 3.0 software. The internal reference was set at δ_C/δ_H 39.5/2.49 ppm (DMSO solvent peak). Two-dimensional heteronuclear single-quantum coherence (HSQC) spectra of LNP samples were recorded as described previously (Cheng et al., 2019; Mansfield et al., 2012; Wang et al., 2019a). ^{31}P NMR spectra were recorded on a Bruker Advance III 600 MHz spectrometer (Bruker, Kalsruhe, Germany) at 25 °C from the dried samples (20 mg) dissolved in 0.4 mL of pydride-d_5-$CDCl_3$ (v/v, 1.6:1) (Wang et al., 2018).

2.7. Fourier transform infrared spectroscopy (FTIR)

FTIR spectra of neat PVA and nanocomposite films were performed in a Perkin Elmer spectrometer (Waltham, MA). Each spectrum was recorded in a range of 4000−400 cm^{-1} at a resolution of 4 cm^{-1} with thirty-two scans.

2.8. Atomic force and filed emission scanning electron microscopy (FESEM)

The morphologies of the AH-LNPs and PVA/AH-LNP nanocomposite films were characterized using AFM (Workshop, Signal Hill, CA). Colloidal AHF-LNP suspensions were first diluted ten times. A drop of diluted suspension was placed onto a clean mica surface and air-dried overnight at room temperature before AFM imaging. PVA/AH-LNP nanocomposite film was directly fixed on a piece of iron plate for AFM imaging. The curvature radius and vibration frequency of the AFM tip were 10−15 nm and 160−225 kHz, respectively.

FESEM images of PVA/AH-LNP nanocomposite films were taken (Zeiss Sigma 300, German) using an accelerating voltage of 5 kV. Before testing, PVA/AH-LNP nanocomposite films were air-dried in an oven at 50 °C for 48 h. Both the surfaces and cross-sections of these films were coated with gold vapor for imaging.

2.9. X-ray diffraction (XRD) analysis

Crystallization of PVA/AH-LNP nanocomposite were evaluated using a X-ray diffractometer (Bruker D8, German) equipped with Cu Kα radiation (λ = 0.154 nm). The scanning range was 10−60°, and the scanning rate was 10° per min.

2.10. Differential scanning calorimetry (DSC)

Glass transition temperatures (T_g) of the PVA/AH-LNP nanocomposite films were determined using a DSC (Q100, TA Instruments, New Castle, DE). Each 3−5 mg film sample was set on a hermetic pan and went through standard heat–cool–heat cycles at a scan rate of 10 °C/min in a range of -50 – 200 °C and purged with nitrogen at a flow rate of 50 mL/min.

2.11. Thermogravimetric analysis (TGA)

The thermal stability of PVA/AH-LNP nanocomposite samples was investigated using a Pyris 1 TGA (Perkin-Elmer, Inc., Waltham, MA) in nitrogen. Samples of approximately 8−10 mg were heated to 700 °C at a heating rate 20 °C/min. Samples were air-dried at 50 °C for 12 h before testing.

2.12. UV blocking analysis

2 mL of PVA/AH-LNPs mixture (before casting) was added into a quartz cuvette. Transmittance measurements were carried out using an Agilent 8453 spectrophotometer (Palo Alto, CA). Each sample was recorded in a range of 200–900 nm three times.

2.13. Contact angle (CA) measurements

The CA of PVA composites were determined through imaging (Attension Theta, Biolin Scientific, Gothenburg, Sweden). A water drop of 2 μL was dropped onto a composite film and photographed after 5 s.

2.14. Mechanical testing

The mechanical properties of PVA nanocomposite films were tested on a Instron Universile Testing Machine 5565 with a 100 N load cell. Before testing, these films were pre-conditioned at 30 % relative humidity (RH), 27 °C for 48 h. Each film was cut into two specimens (90 by 15 mm) for testing. Specimens were weighed prior to testing. The grips were separated at a rate of 30 mm/min with a initial gauge length of 70 mm. Tensile tests were performed after re-condititioning to 50 % RH, 23 °C for 24 h. To assess the significance of *p*-TsOH and LNP levels on toughness, parametric and non-parametric analysis of vaiance (ANOVA) methods were applied. In particular, the amounts of *p*-TsOH and LNP were varied as explanitory variables, and stiffness, failure strain, tensile strength, and toughness were measured as response variables. No interaction between the explanitory variables was assumed.

2.15. Biodegradation by mold and decay fungi

Two mold fungi, Aspergillus niger 2.242 provided by University of Virginia, and Trichoderma atraviride ATCC 20476 were grown on 2% malt agar (Difco, Detroit, Mi. USA) for 2 weeks. Spores suspensions were prepared by washing the surface of each malt agar plate with 10−15 mL of sterile deionized water (DI) according to ASTM Standard D4445−91 (ASTM, 1998). Each mold spore suspension was transferred to a spray bottle and diluted to 100 mL with DI water to yield 3 × 107 spores/mL. The spray bottle was adjusted to deliver 1 mL inoculum per spray on the test samples. Two wood decay fungi, Postia placenta (Fr.) M.Lars and Lomb. (MAD 698) and Phanerochaete chrysosporium (ME 461) were obtained from the Forest Products laboratory, Madison, Wisconsin, and were grown on 2% malt agar, at 27 °C and 80 % relative humidity (RH) for 2 weeks prior to placing the test samples on the agar plates.

Following the guidelines of AWPA Standard E10−12 (AWPA, 2014), test samples were weighed and placed on the malt agar plates containing a confluent growth of decay fungi. On the 12th week, fungal mycelia and mold coverage were brushed from the specimens. Specimens were oven-dried, reconditioned at 27 °C and 80 % RH and reweighted. Percentage mass loss was calculated for each specimen and reported as an average for each specimen group.

2.16. Water vapor permeability (WVP)

The PVA/AH-LNP nanocomposite films were conditioned at 21.1 °C and 50 % RH for two weeks prior to conducting WVP tests. WVP was determined gravimetrically following the desiccant method according to ASTM E96 using a 68–3000 EZ-Cup vapometer assemblies (Thwing-Albert Instrument Company, West Berlin, NJ, USA)

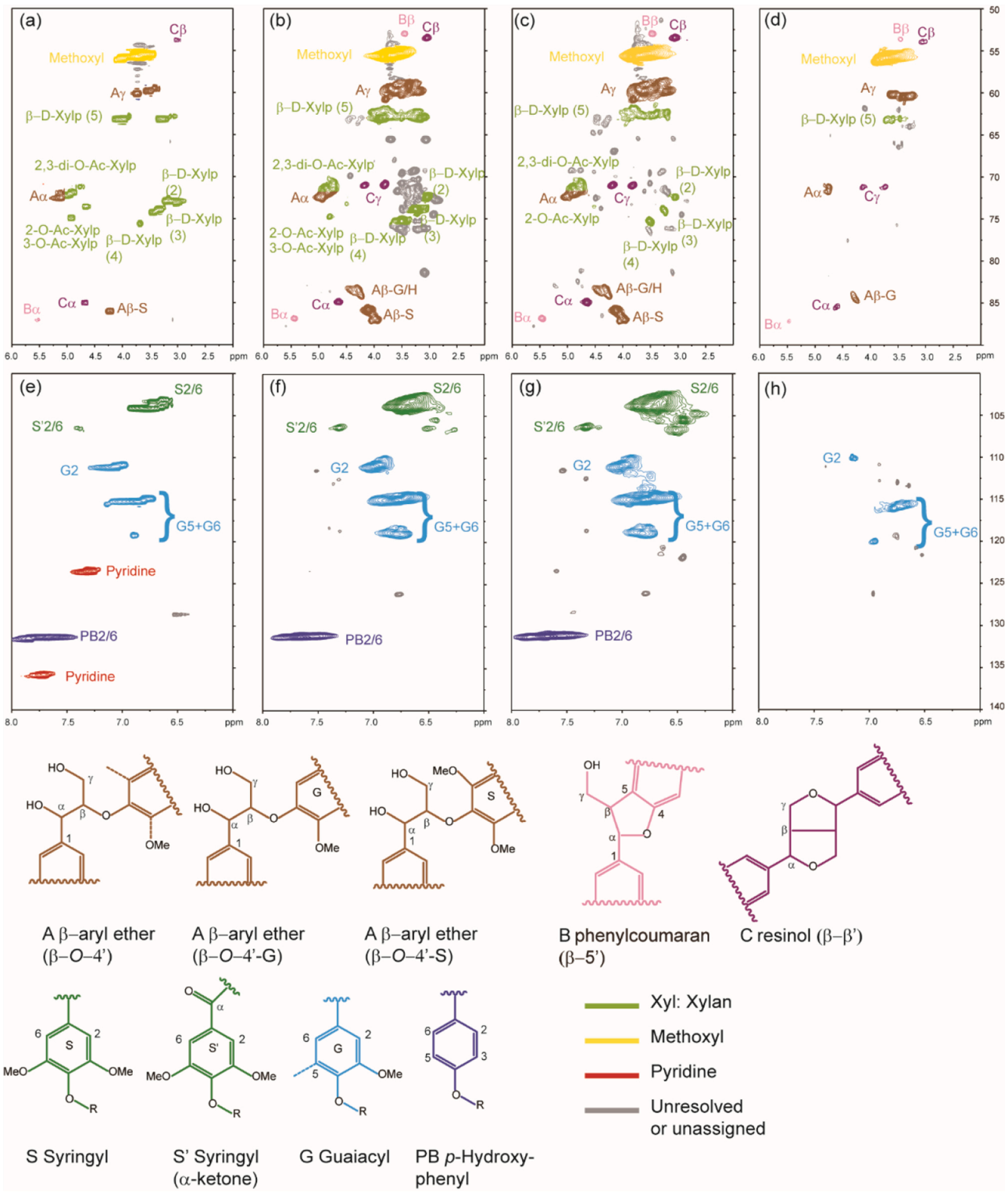

Fig. 1. 2D ^{13}C-^{1}H NMR analyses of lignin samples showing side-chain and aromatic regions of the while cell wall (WCW) (a and e), lignin from P15T80t60 (b and f), P40T80t60 (c and g), and alkali lignin (d and h).

3. Results and discussion

3.1. Compositions of the colloidal AH-LNP suspensions

As listed in Table 1, the colloidal AH-LNP suspensions from the *p*-TsOH spent liquor used for making PVA nanocomposites contained a small amount of xylose and glucose, as well a relatively large amount of *p*-TsOH. The dissolved carbohydrates can be in the form of monomeric and oligomer sugars. Oligomers were not determined. The glucose concentrations in the supernatants of the diluted spent liquors were near the detection limit. High severity AHF using a high *p*-TsOH concentration of 40 wt% resulted in a high xylose concentration of 0.56 g/L. The amounts of LNPs were determined indirectly from the balance of the total amount of lignin dissolved during an AHF and the amount of lignin

Table 2
The relative quantities of substructures and subunits in the WCW and LNPs in the colloidal AH-LNP suspensions.

	WCW	PW15	PW40	Alk15
Lignin interunit linkages (results expressed per 100Ar)				
β-O-4′	84.7	73.9	53.4	18.0
β-5′	3.6	1.6	1.5	ND
β-β’	ND	5.0	6.4	2.8
Lignin aromatic units [0.5S + G = 100 %]				
S (%)	56.4	66.5	75.6	ND
G (%)	43.6	33.5	24.4	100
S/G	1.3	2.0	3.1	ND

ND stands for not detectable.

precipitated through dilution to a given *p*-TsOH concentration as listed in Table 1. The colloidal AH-LNP suspensions from batch dissolution of alkaline lignin were also used to produce PVA/AH-LNP nanocomposites.

3.2. LNP chemical structure and morphology

The chemical structures of the LNPs from AHF of poplar wood and alkali lignin along with the poplar wood whole cell wall (WCW) were investigated by 2D NMR. The side-chain and aromatic regions of 2D HSQC spectra, and the main substructures of lignin are shown in Fig. 1. The assignment of main cross-peaks was according to literature (Del Río et al., 2012; Kim and Ralph, 2010; Wen et al., 2015), and the relative quantities of main substructures from the integration of ^{1}H-^{13}C correlation peaks in the HSQC spectra are shown in Table 2. The S/G ratio of the poplar wood lignin could reveal the extent of delignification process (González-Vila et al., 1999; Lourenço et al., 2012). As S/G ratio increased from 1.3 (WCW) to 2.0 with *p*-TsOH of 15 wt%, and further increased to 3.1 under *p*-TsOH 40 wt%.

With respect to lignin side-chain linkages, the relative contents of β-*O*-4′ and β-β’ substructures in the WCW were 84.7 % and 3.6 %, respectively, while the β-5′ could not be detected. Fractionations under *p*-TsOH concentration of 15 and 40 wt%, the relative content of β-*O*-4′ in the resultant LNP samples was 73.9 % and 53.4 %, respectively, suggesting the cleavage and condensation of β-*O*-4′ (Cai et al., 2020; Chen et al., 2017; Wang et al., 2019b). In comparison, the relative contents of β-*O*-4′ in the alkali lignin was only 18.0 %, indicating significant condensation of alkali lignin taking place during wood pulping (Adler and Wesslén, 1964; Rinaldi et al., 2016). AFM images reveal that the AH-LNPs in the colloidal LNP suspensions have diameters approximately from 50 to 250 nm (Fig. 2A-D). Particle aggregation was minimal. The thicknesses of these AH-LNPs are also determined from AFM topographic measurements of approximately 3−4 nm (Fig. 2E), suggesting that AH-LNPs have a morphology of oblate spheroid or circular disk, in agreement with previous studies (Bian et al., 2017; Chen et al., 2017; Ma et al., 2018). Furthermore, the morphologies of the LNPs from different fractionation conditions using both poplar wood and alkali lignin are not much significantly different with the LNPs from alkali lignin is slightly thinner (Fig. 2E). Therefore, we will not differentiate poplar wood LNPs from different fractionation conditions in the following discussion.

3.3. PVA/AH-LNP nanocomposite tensile strength and toughness

The effect of colloidal AH-LNPs on the tensile strength of PVA nanocomposites is shown in Fig. 3A. It has been reported that the addition of non-colloidal LNPs into PVA had no obvious effects on PVA composite film tensile strength and tensile strain (Tian et al., 2017). Adding *p*-TsOH alone substantially increased PVA composite film strain, i.e., the mean tensile strain at break of a low-Mw (89,000–98,000 Da) PVA film, LM-PVA-pTsOH28, was increased from 108 % to 232 % at *p*-TsOH loading of 28.5 % of dry weight PVA (Table 3). Here the labeling for the PVA films are self-explanatory, i.e., LM- and HM-PVA stand for low-Mw and high-Mw PVA, respectively, pTsOH*xx* represent loading of p-TsOH in *xx* wt% of PVA. Specific tensile strength was decreased. Similar effects were also observed from the film, HM-PVA-pTsOH42, made of high-Mw (130,000 Da) PVA (Table 3) at *p*-TsOH loading of 42 wt% of PVA.

With the addition of colloidal poplar wood AH-LNP at 0.69 wt% of PVA under the same *p*-TsOH loading, the mean failure tensile strain of the resultant PVA-LNP composite film, LW-PVA-pTsOH28-PLNP069, was further increased from 232 % for LW-PVA-pTSOH28 without LNP to 284 % (Table 3, also example of single film shown in Fig. 3A). Here the extended labeling -PLNP069 stands for polar wood LNP with loading at 0.69 wt% of PVA. The tensile strength of the PVA-LNP composite film

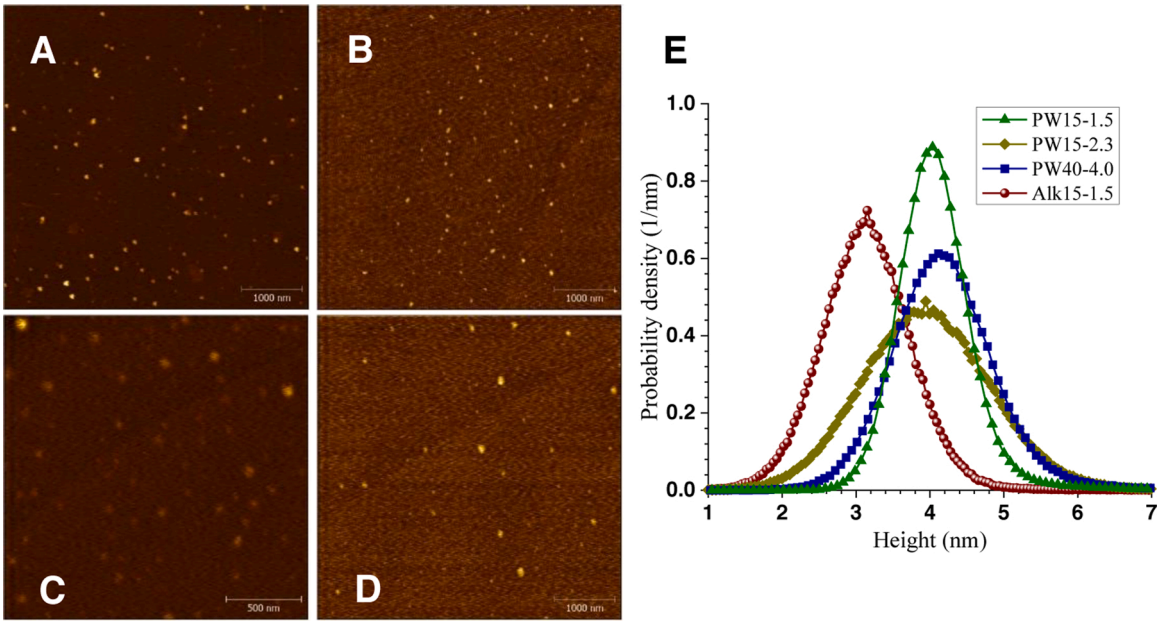

Fig. 2. AFM images of AH-LNPs in the supernatants of diluted spent liquors: PW15-1.5 (A), PW15-2.3 (B), PW40-4.0 (C), and Alk15-1.5 (D). E: AFM-measured topographical height distributions of AH-LNPs.

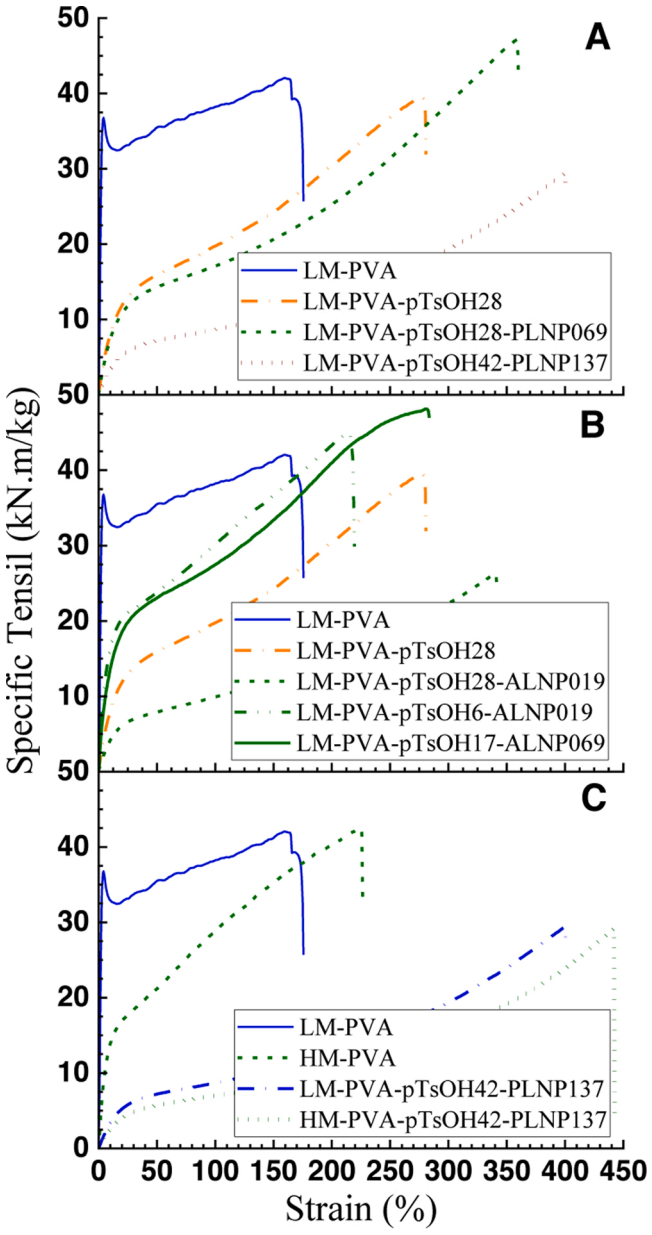

Fig. 3. Examples of tensile strength curves of single PVA/AH-LNP nanocomposite film.

was not affected. Increasing *p*-TsOH or LNP loading improved failure strain, but increasing *p*-TsOH reduced specific tensile strength for both the LMw and HMw PVA composite films, as can be seen by comparing LW-PVA-pTsOH28-PLNP069 with LM-PVA-pTsOH42-PLNP137 and HM-PVA-pTsOH42-PLNP137 (Fig. 3B, Table 3). Using high-Mw PVA did not affect mean failure strain or tensile strength for both the neat PVA and PVA-LNP composite films (Table 3 and Fig. 3B).

Using colloidal AH-LNP suspensions from alkali lignin, we were able to increase the relative loading of LNP while reducing *p*-TsOH loading to improve tensile strength and maintain high failure strain for producing films with high toughness. For example, LM-PVA-pTsOH6-ALNP019 and LM-PVA-pTsOH17-ALNP069 (ALNPnyy stands for alkali LNP loading of n.yy wt% of PVA), had LNP/*p*-TsOH loading ratios of 0.032 and 0.041, respectively, achieved not only greater mean failure strain than that of the neat PVA film, but also comparable mean specific tensile strength to that of the neat PVA film LM-PVA (Table 3, also Fig. 3C). Among the three alkali LNP PVA films produced, LM-PVA-pTsOH17-ALNP069, with the greatest LNP/*p*-TsOH ratios of 0.041 has the greatest tensile strength.Comparing with LM-PVA-pTsOH28-PLNP069, LM-PVA-pTsOH17-ALNP069 with a lower *p*-TsOH loading had a higher tensile strength and lower failure strain. Therefore, future study should focus on reducing *p*-TsOH loading while maintaining a stable LNP suspension for composite applications.

Material toughness is determined by both the failure strain and tensile strength. Adding *p*-TsOH alone did not increase PVA film toughness (Table 3, Fig. S1) despite a substantial increase in mean failure strain (Table 3). When adding colloidal AH-LNP in aqueous *p*-TsOH, depending on the effect of LNP on mean tensile strength and the effect of *p*-TsOH on mean failure film strain, the toughness may have remained the same as that of PVA/*p*-TsOH film (Table 3). However, at a relatively low *p*-TsOH loading of 6% and LNP loading of only 0.19 %, mean toughness of LM-PVA-pTsOH6-ALNP019 was increased by 25 % over its corresponding neat film LM-PVA and failure strain increased by over 60 %. A smaller increase of 12 % was observed for LM-PVA-pTsOH17-ALNP069 at a high *p*-TsOH loading (Fig. S1, Table 3). Please refer to Support Information for statistical analyses of the effects of *p*-TsOH and LNP on film toughness and failure strain (Figs. S2 and S3, Tables S1 and S2).

Several PVA/LNP films have comparable failure strains (Table 3) to that of film made of PVA/LA of approximately 300 % (Zhang et al., 2019). However, the toughness of PVA/LA nanocomposites were much higher than the results reported in this study. This is probably due to the fact that there are only π-π stacking and weak hydrophobic interaction between LNPs and *p*-TsOH to merely form a complex or aggregate, unlike LA as a molecule with much stronger chemical bonds in its inner structure. Furthermore, excess *p*-TsOH could crystallize during drying and result in pores or defects to decrease film tensile strength. The increased crazing can be seen from the increases in water vapor permeability from 0.033 g/s/m/Pa for neat LM-PVA to 1.18 g/s/m/Pa for LM-PVA-pTsOH28-PLNP069, and to 2.99 g/s/m/Pa for LM-PVA-pTsOH42-PLNP137 with a higher *p*-TsOH loading of 42 % (Table S1).

3.4. Morphology and hydrophobicity of PVA/AH-LNP nanocomposites

Neat PVA surface is rather smooth as shown in Fig. 4A1 and B1. Crystalized structure of large *p*-TsOH patches were present on the surface of the film LM-PVA-pTsOH28 as shown in Fig. 4A2 and B2, while smaller and more homogeneously distributed particles were present on the surface of the composite film LM-PVA-pTsOH28-PLNP069 (Fig. 4A3 and B3). This was probably related to the formation of micellar-like aggregates (complexes) between *p*-TsOH and LNPs, which could increase the compatibility between PVA and *p*-TsOH. By comparing the surface SEM micrographs of the film LM-PVA-pTsOH28-PLNP069 before (Fig. 4B3) and after tensile test (Fig. 4B4), it is clear that the surface of the film after stretching became rougher. The cracks are clearly visible from the SEM cross sectional micrograph after test (Fig. 4C4). These probably resulted from the deformation or breakage of the LNPs aggregates or the hydrogen bonding between PVA and LNP aggregates as will be discussed later.

The improved surface hydrophobicity of PVA/AH-LNP nanocomposite film due to the addition of LNPs can be evaluated from their contact angles (CA) with water (Fig. 4D1-D4, Table S3). CA was increased from 44.1° for the neat LM-PVA film to 52.7° for LM-PVA-pTsOH28 with the application of *p*-TsOH alone due to the presence of a hydrophobic end in *p*-TsOH, and further increased to 56.2° for LM-PVA-pTsOH28-PLNP069 with a higher LNP loading. Besides, the contact angle of the film LM-PVA-pTsOH28-ALNP019 (CA, 55.1°) was lower than that of the film LM-PVA-pTsOH28-PLNP069, indicating that a high LNP content was beneficial for increasing hydrophobicity of the PVA nanocomposite films.

Table 3
List of PVA films produced in this study and their mechanical properties.

Samples[1]	PVA (g)	Colloidal AH-LNP	*p*-TsOH (wt% PVA)	LNP (wt % PVA)	Average GSM (g/m^2)	Average weight (g)	Failure Strain (%)	Specific stress (kN m/kg)	Stiffness (kN m/kg)	Toughness (kN m/kg)
LM-PVA	1.25	N/A	0	0	99 ± 11	0.9078	108 ± 47	38.6 ± 2.0	1279 ± 110	37.8 ± 17.5
HM-PVA	1.25	N/A	0	0	115 ± 9	1.052	103 ± 62	30.8 ± 5.8	437 ± 170	26.3 ± 18.3
LM-PVA-pTsOH28	1.25	*p*-TsOH1.5	28.5	0	142 ± 6	1.2285	232 ± 31	22.8 ± 2.4	44 ± 3	33.0 ± 6.6
HM-PVA-pTsOH42	1.25	*p*-TsOH2.3	42.8	0	169 ± 12	1.548	372 ± 36	19.5 ± 4.1	15 ± 2	31.8 ± 6.8
LM-PVA-pTsOH28-PLNP069	1.25	PW15−1.5	28.5	0.69	143 ± 13	1.3111	284 ± 44	21.9 ± 3.8	36 ± 1	36.2 ± 9.8
LM-PVA-pTsOH42-PLNP137	1.25	PW15−2.3	42.8	1.37	153 ± 7	1.3993	344 ± 54	15.0 ± 3.4	17 ± 1	27.8 ± 7.9
HM-PVA-pTsOH42-PLNP137	1.25	PW15−2.3	42.8	1.37	172 ± 8	1.5709	382 ± 41	18.5 ± 3.7	14 ± 1	31.5 ± 6.5
LM-PVA-pTsOH28-ALNP019	1.25	Alk15−1.5	28.5	0.19	143 ± 9	1.3047	308 ± 32	15.4 ± 2.6	24 ± 2	27.2 ± 5.6
LM-PVA-pTsOH6-ALNP019	1.25	Alk15L	6.5	0.19	117 ± 11	1.067	175 ± 49	34.5 ± 2.5	486 ± 204	47.3 ± 11.3
LM-PVA-pTsOH17-ALNP069	1.25	Alk15H	17.3	0.69	136 ± 11	1.2405	226 ± 29	27.8 ± 2.0	96 ± 9	42.3 ± 8.2

[1] Sample labeling: LM- and HM-PVA stand for low-Mw and high-Mw PVA, respectively; pTsOHxx stands for *p*-TsOH loading in xx wt% of PVA; PLNPnyy and ALNPnyy stand for polar wood and alkali LNP, respectively, loading at n.yy wt% of PVA.

3.5. Mechanism of PVA/AH-LNP nanocomposite strength enhancement

The colloidal AH-LNP suspension is formed first by the hydrophobic interaction between the nonpolar part (toluene moiety) of the *p*-TsOH molecule and lignin to result in simple *p*-TsOH/LNP complexes (Fig. 5A), then through π-π stacking of the toluene moiety in these simple complexes to result in *p*-TsOH/LNP aggregates, especially under high *p*-TsOH concentrations (> MHC) through drying (Fig. 5A). This aggregation makes solubilizing hydrophobic LNPs in aqueous system possible and results in a stable colloidal *p*-TsOH/AH-LNP suspension.

When adding *p*-TsOH to PVA alone, the SO_3H end in *p*-TsOH will form hydrogen bonding with the PVA hydroxyl groups to attach to a PVA chain (Fig. 5B). This hydrogen bonding can improve PVA molecular chain alignment by reducing hydrogen bonds among PVA chains which tend to create disoriented PVA molecular chains. This explains why adding *p*-TsOH alone significantly improved PVA failure strain but reduced tensile strength. Similarly, the SO_3H ends of *p*-TsOH/AH-LNP aggregates can also form intermolecular hydrogen bonding with PVA molecular chains (Fig. 5C). The difference is that *p*-TsOH/AH-LNP aggregates can bind at least two PVA chains together due to the presence of SO_3H groups surrounding the entire outer layer of *p*-TsOH/AH-LNP aggregates (Fig. 5C), rather than simply attached to one chain with *p*-TsOH alone (comparing Figs. 5B with 5C). Under tension, the *p*-TsOH/AH-LNP aggregates can break due to the weak hydrophobic interactions (Fig. 5D), but can reform which not only improved composite tensile strength but also significantly increased ductility. This mechanism is similar to the concept of "sacrificial hydrogen bonding" that can break and reform for explaining strength and toughness enhancement by adding LA into PVA (Zhang et al., 2019). The difference is that the hydrophobic interaction between PVA and *p*-TsOH/AH-LNP aggregates is weaker than the sacrificial hydrogen bonding. As a result, tensile increase observed in the present study is less significant than that using LA (Zhang et al., 2019). The nanophase separation between PVA chains created by the *p*-TsOH/AH-LNP aggregates can prevent the growth of crazing to improve tensile strength and strain.

To verify the existence of the above mentioned hydrogen bonding between PVA and colloidal *p*-TsOH/AH-LNP complexes, the PVA/AH-LNP composite films were analyzed by FTIR (Zhang et al., 2019). As shown in Fig. 6A, the absorption band centered at 3271 cm^{-1} corresponds to O—H stretching vibrations in the neat LM-PVA film. With the addition of *p*-TsOH alone, the O—H absorption blue shifted to 3280 cm^{-1} (LM-PVA-pTsOH28). Similar shifts were also observed for PVA/AH-LNP composite samples. The shift was increased with increasing *p*-TsOH concentration, e.g., the peak was shifted to 3292 cm^{-1} for the film LM-PVA-pTsOH42-ALNP137 with the highest *p*-TsOH loading, compared with 3284 cm^{-1} for LM-PVA- pTsOH28-PLNP069. The 4 cm^{-1} difference in shift between LM-PVA-pTsOH28 and LM-PVA-pTsOH28-PLNP069 may be attributed to lignin, because lignin contains a small amount of hydroxyl groups as analyzed by ^{31}P NMR (Table S4) which may contribute to the signal shift. The absorption peak for S═O in the PVA-pTsOH film (*p*-TsOH alone) at approximately 1032 cm^{-1} had no obvious shift after adding LNPs comparing with the FTIR spectra of the PVA/AH-LNP nanocomposites, further confirming that hydrogen bonding interaction is mainly taking place between PVA and *p*-TsOH.

X-ray diffraction (XRD) study further verifies hydrogen bonding between PVA and colloidal *p*-TsOH/AH-LNP complexes. The diffractograms of PVA/AH-LNP nanocomposites exhibit a peak at $2\theta = 19.4^\circ$ and a shoulder at $2\theta = 22.5^\circ$, corresponding to the characteristic signals of semi-crystalline PVA (Liang et al., 2009). The intensity of the two diffraction signals were almost unchanged in all PVA/AH-LNP nanocomposites. No sharp diffraction peaks from *p*-TsOH were observed from LM-PVA-pTsOH28, LM-PVA-pTsOH28-PLNP069, LM-PVA-pTsOH28-ALNP069. This indicates that *p*-TsOH and AH-LNPs can be homogeneously dispersed into the PVA matrix and would not significantly affect the crystallinity of PVA matrix. Compared with the neat PVA film, the new diffraction weak peak at $2\theta = 40.2^\circ$ appeared for the PVA/*p*-TsOH-AHF-LNP nanocomposite films. Using the Bragg's equation, $d = \lambda/(2sin\theta)$ with $\lambda = 0.154$ nm and $2\theta = 40.2^\circ$, the distance between *p*-TsOH and PVA molecular chains is determined at 0.224 nm, consistent with the hydrogen-bonding interaction distance 0.225 nm. This further confirmed the hydrogen-bonding interaction between *p*-TsOH/AHF-LNP aggregates and PVA matrix. Furthermore, introducing a

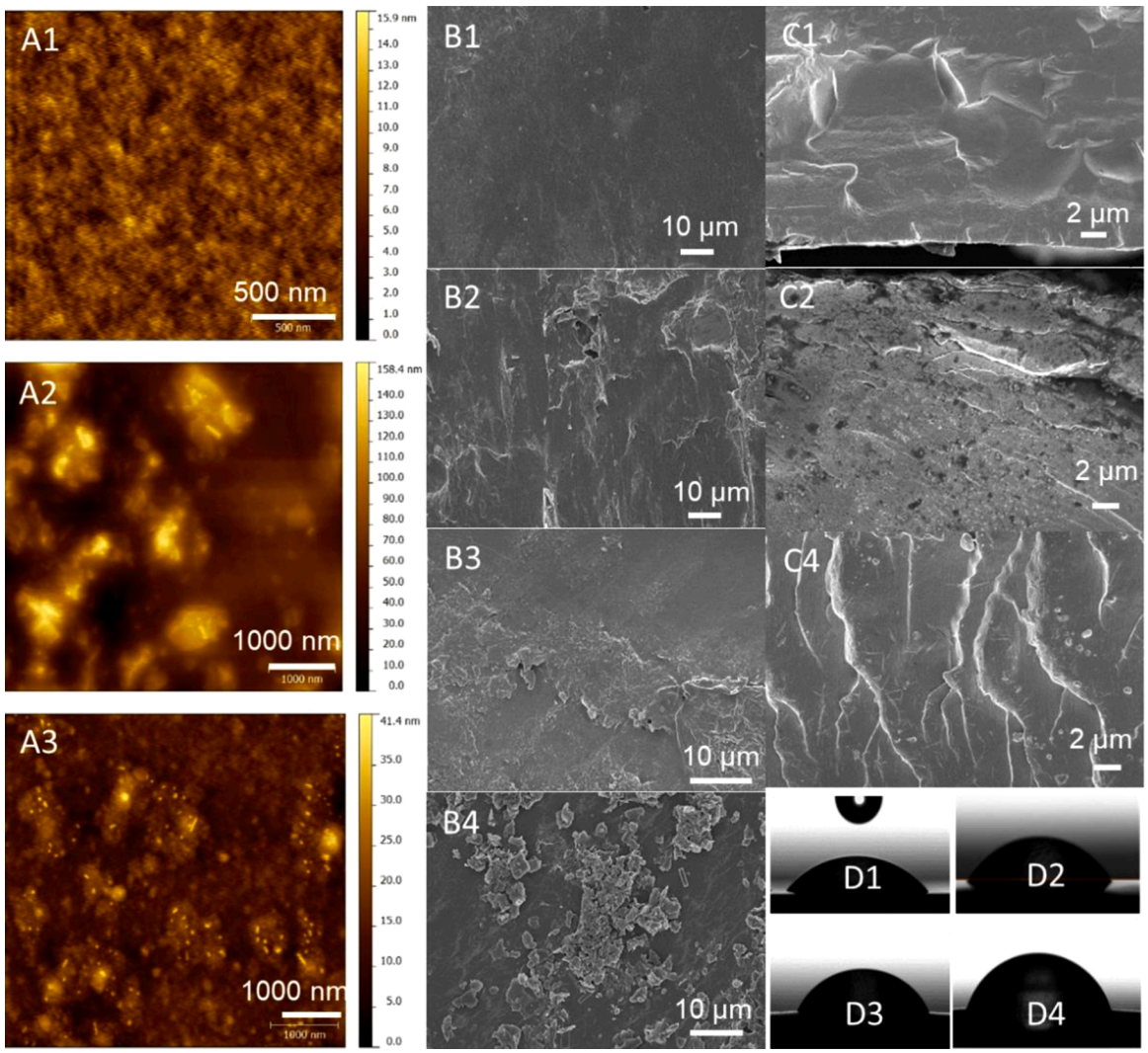

Fig. 4. PVA/AH-LNP nanocomposite film morphology. A: surface AFM images, B: surface SEM micrographs, C: cross sectional SEM micrographs, 1: Neat LM-PVA, 2: LM-PVA-pTsOH28, 3 and 4: LM-PVA-pTsOH28-PLNP069 before and after tensile test, respectively. D: Contact angles of neat LM-PVA (D1), LM-PVA-pTsOH28 (D2), LM-PVA-pTsOH28-PLNP069 (D3), and LM-PVA-pTsOH28-ALNP019 (D4).

proper amount of *p*-TsOH and AH-LNPs decreased the crystallization of PVA matrix (Table S3). However, sharp diffraction peaks were observed from the sample LM-PVA-pTsOH42-PLNP137 with *p*-TsOH loading of 42 wt%, suggesting excessive *p*-TsOH could crystallize in the nanocomposites. Therefore, the great failure strain of LM-PVA-pTsOH42-PLNP137 (Fig. 3A and C, Table 3) is possibly related to crystal slip during film stretching (Hiss et al., 1999). The crystallization of excessive *p*-TsOH in PVA/AH-LNP nanocomposites could also result in reducing specific tensile stress, stiffness, and therefore toughness.

The hydrogen bonding mechanism could be used to explain the effects of the two kinds of lignin nanoparticles use in the president study on PVA/AH-LNP nanocomposite properties. ^{31}P NMR analysis (Table S4) indicates that the hydroxyl group content of lignin PW40 was 4.05 mmol/g, slightly lower than 5.00 mmol/g for alkali lignin. However, the aliphatic hydroxyl content in PW40 was 63 %, almost double the value of 35 % for alkali lignin. The greater hydroxyl group content is beneficial to form more hydrogen bonds, resulting in a greater tensile strength. However, the condensed structure in lignin as revealed by the amount of β-O-4 linkages from 2D NMR analysis as listed in Table 2 is closely related to the amount of condensed hydroxyl content (Table S4) in lignin nanoparticles. As a result, lignin condensation during AHF and alkaline pulping could limit the formation of hydrogen bonds between PVA and AH-LNPs during the stretching process to decrease tensile strain of PVA/AH-LNP nanocomposites. Based on the extent of hydroxyl group condensation (Table S4), this effect is more pronounced for PVA/AH-LNP nanocomposites made of Alkali LNPs than for poplar wood LNPs. This explains the lower tensile strain PVA/AH-LNP nanocomposites made of Alkali LNPs as shown in Fig. 2 and Table 3.

3.6. PVA/AH-LNP nanocomposite water permeability, thermal stability, and processibility

The decreased hydrogen bonding by *p*-TsOH and the presence of nanoscale crazing due to the application of colloidal LNP suspension as discussed earlier resulted in a more porous composite film than neat PVA. This increased water vapor permeability (Table S1). Besides, the crystallization of excessive *p*-TsOH in PVA/AH-LNP nanocomposite such as LM-PVA-pTsOH42-PLNP137 as discussed above may also resulted in weak interfacial interactions between the fillers, i.e., *p*-TsOH and LNPs, and PVA to increase water vapor permeability. *p*-TsOH and LNP loading have a significant effect on increasing permeability. It appears alkaline LNPs had a stronger effect than LNPs from fractionated poplar wood.

The application of *p*-TsOH also negatively affected the thermal stability of PVA nanocomposites (Fig. S4). The onset thermal degradation temperature (T_{on}) was decreased from 300.5 °C for the neat film LM-

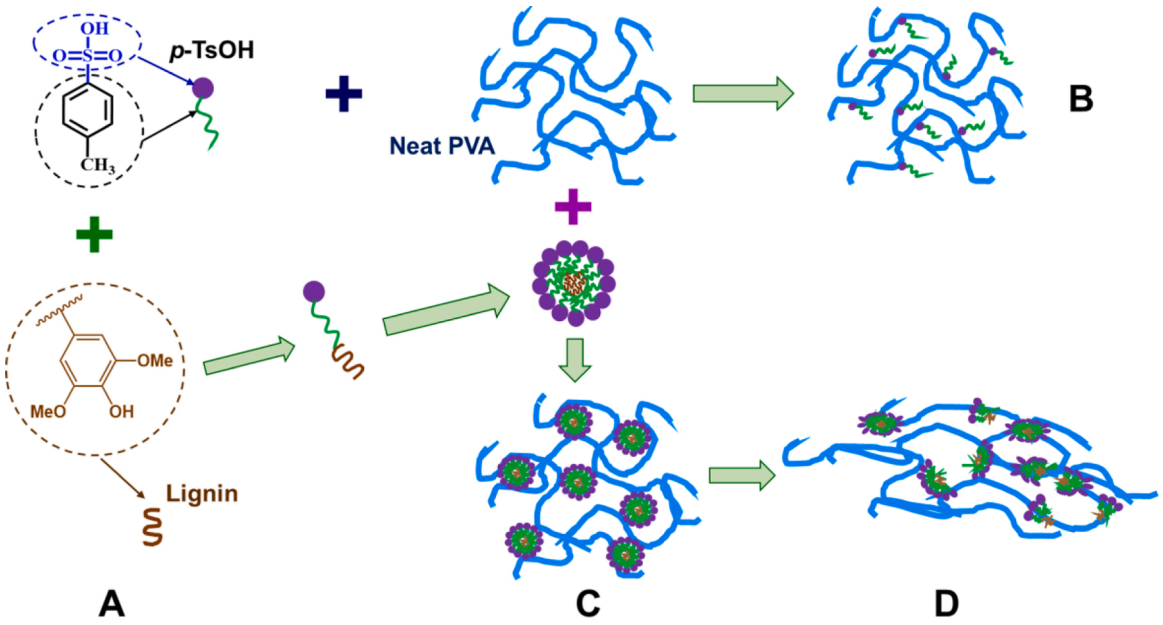

Fig. 5. Proposed mechanism of colloidal AH-LNPs enhancing the mechanical properties of PVA/AH-LNP nanocomposites. A: Formation of *p*-TsOH/LNP complexes and aggregates; B: *p*-TsOH hydrogen bonding with PVA; C: Forming PVA/AH-LNP composites; D: PVA/AH-LNP composite under tension.

PVA to below 200 °C of the PVA nanocomposite films depending on *p*-TsOH and LNP loadings (Table S2). Comparing the samples with the same or similar *p*-TsOH loadings, the results clearly indicated the increase in *p*-TsOH reduced film thermal stability. Increasing LNP loading led to the increased thermal stability of PVA nanocomposite, in agreement with literature work (Nair et al., 2014). *p*-TsOH also had an obvious effect on the glass transition temperature (T_g) of PVA nanocomposite films, as evidenced by large increase in the T_g from 76.9 °C for the neat PVA film LM-PVA to approximately 102 °C for the PVA nanocomposite films (Table S2). This increase was probably due to the strong intermolecular hydrogen bonding interactions between *p*-TsOH and PVA which limits the movement of PVA chains (Nair et al., 2014; Zhang et al., 2019).

3.7. PVA/AH-LNP nanocomposite optical properties

The UV blocking capability of PVA/AH-LNP nanocomposite films was evaluated by measuring their transmittance spectra in the UV–vis range as shown in Fig. 7. The neat PVA film LM-PVA showed excellent transparency (100 %) at wavelength > 400 nm and limited UV protection in UVA and UVB with transmittance greater than 60 % between 275–400 nm (Fig. 7A). Adding *p*-TsOH alone resulted in complete UVC (< 275 nm) protection, and provided some degree of UVB protection. Adding colloidal AH-LNPs achieved near complete protection of UVB and good UVA protection. As an example, the film LM-PVA-pTsOH42-ALNP137 could shield 100 % of the UVC, 100 % of the UVB, and more than 50 % of the UVA. The PVA nanocomposites also showed good transparency, as evidenced by the light transmittance over 80 % in the visible light region (400−760 nm). The UV blocking capacity of the film LM-PVA- pTsOH42-ALNP137 with 1.37 wt% LNPs was similar to that of the PVA nanocomposite without *p*-TsOH at 4% LNPs (Tian et al., 2017), indicating the UV-blocking effect of *p*-TsOH. It has been previously reported that LNPs could absorb photon energy and convert it to heat with the corresponding hydrophilic chromophores (including phenolic hydroxyl, carbonyl, and carboxyl groups) to shield the ultraviolet light (Wang et al., 2016; Xiong et al., 2014). Quantitative ^{31}P NMR analysis (Table S2) showed that the contents of phenolic hydroxyl and carboxyl of AHF-LNPs were lower than those of alkali lignin. However, the film LM-PVA-pTsOH28-PLNP069 had better UV shielding property than that of the LM-PVA-pTsOH28-ALNP019. This indicated that the LNP content plays an important role in UV shielding performance. In general, PVA/AH-LNP nanocomposite films showed efficient UV blocking capacity without affecting its visible light transparency (Yang et al., 2016). After 4 times of reproduction, the PVA nanocomposites still showed relatively high transparency and great UV blocking performance, as shown in Fig. 7B.

3.8. PVA/AH-LNP nanocomposite biodegradability

The biodegradability is of great importance (Gross and Kalra, 2002; Ren, 2003). The biodegradability of PVA/AH-LNP nanocomposites was evaluated using four common microorganisms, *Aspergillus niger* (*A. niger*. mold), *Trichoderma atraviride* (*T. atraviride*, mold), *Postia placenta* (*P. placenta*, fungi), and *Phanerochaete chrysosporium* (*P. chrysosporium*, fungi). Both mold and fungi had grown well to cover the surfaces of the samples except neat PVA on day 14 (Fig. S5). The weight loss of neat LM-PVA film, LM-PVA-pTsOH28-PLNP069, and LM-PVA-pTsOH43-LNP034 after 12 weeks are listed in Table 4. The results indicate that the four microorganisms used here were not able to effectively biodegrade PVA. It was known that PVA is biodegradable only by selected microorganisms that do not commonly present in a natural environment (Chiellini et al., 2003). Adding *p*-TsOH did not negatively affect microbe growth but could improve biodegradability. The weight loss of LM-PVA-pTsOH43-LNP034 was higher than that of the film LM-PVA-pTsOH28-PLNP069 with similar polysaccharide content, further suggesting that the high *p*-TsOH content was beneficial to the degradability of PVA nanocomposites. The good biodegradability of PVA/AH-LNP nanocomposite films may be influenced by the polysaccharides (xylose and glucose) in the colloidal LNP system (Table 1) (Saxena and Ragauskas, 2009).

4. Conclusions

Colloidal lignin nanoparticles (LNPs) derived from acid hydrophobic fractionation (AHF) of wood or commercial alkali lignin using *p*-Toluenesulfonic acid (*p*-TsOH) can be used to produce tougher PVA/AHF-LNP composites with better biodegradability, and higher UV blocking performance than those of neat PVA film. The formation of *p*-TsOH/AHF-LNP aggregates and their breakage and reformation under tension, the formation of hydrogen bonding between the SO_3H end of the outer

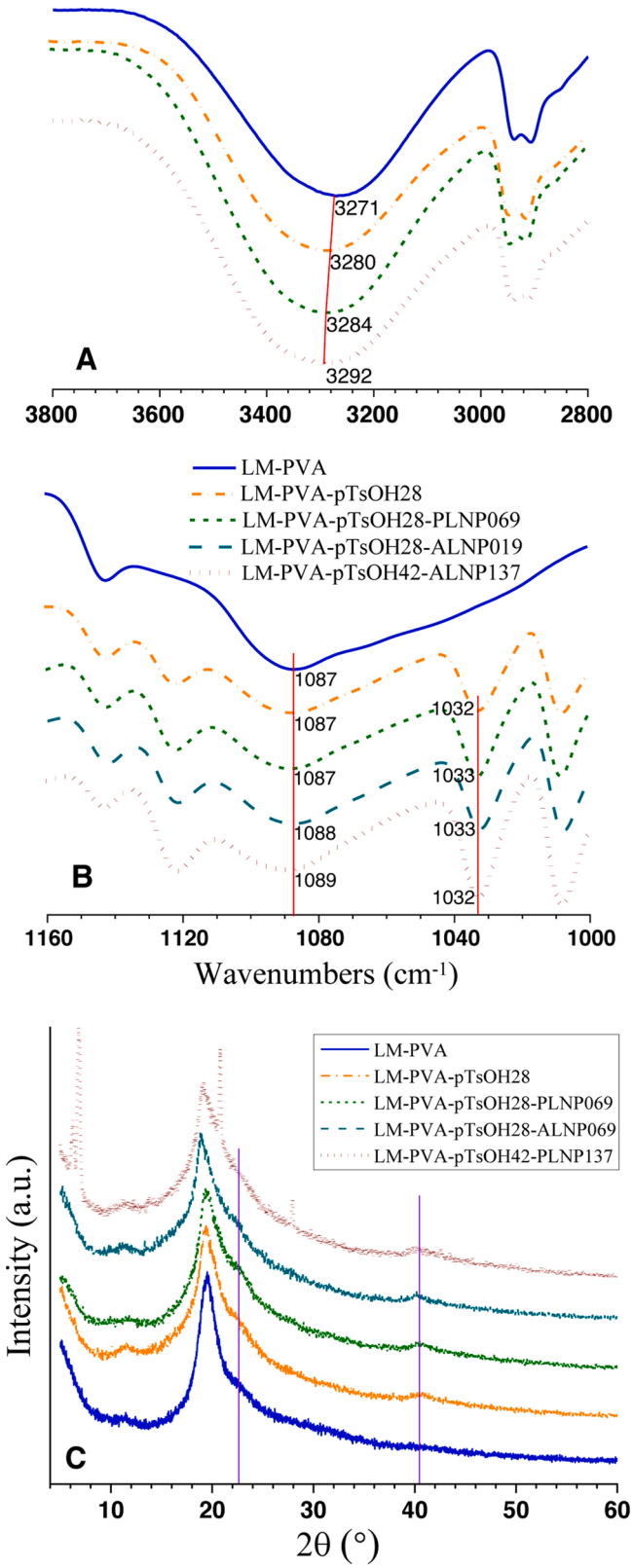

Fig. 6. A and B: FT-IR spectra of PVA/AHF-LNP nanocomposite films showing the differences of O—H (A) and S—O (B) stretching vibrations. C: X-ray diffractograms of PVA/AHF-LNP nanocomposite.

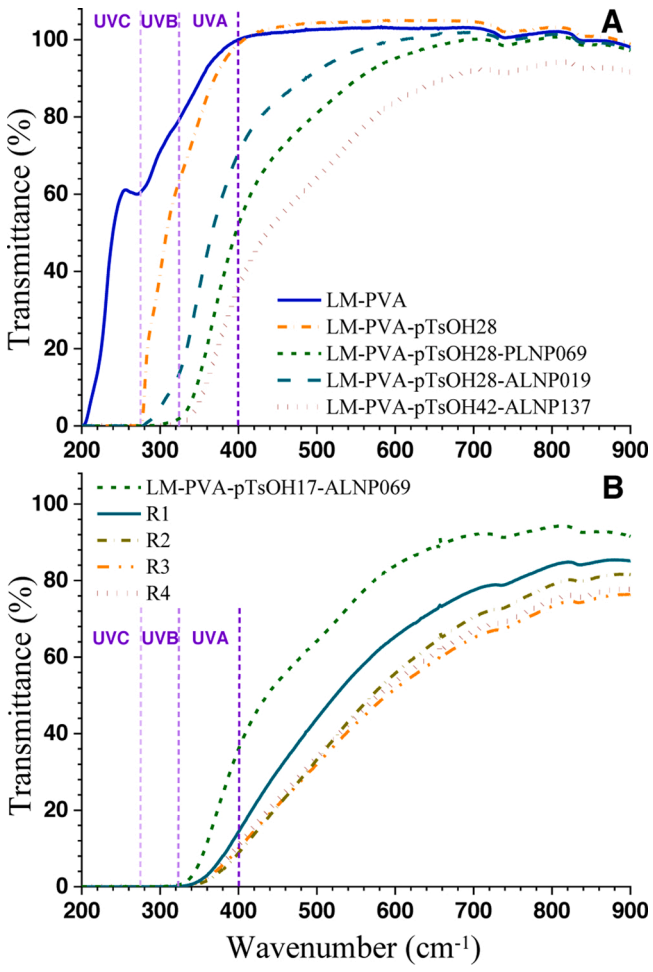

Fig. 7. UV–vis transmittance spectra of PVA nanocomposite films. (A) Effects of *p*-TsOH and LNP; (B): Effect of recycling.

Table 4
The weight loss of samples after biodegradation.

	LM-PVA	LM-PVA-pTsOH28-PLNP069	LM-PVA- pTsOH43-PLNP034
A. niger (%)	0	14.7	39.6
T. atraviride (%)	1.6	11.2	32.7
P. placenta (%)	0	9.8	37.8
P. chrysosporium (%)	2.4	17.2	33.1

A. niger, Aspergillus niger (mold); T. atraviride, Trichoderma atraviride (mold); P. placenta, Postia placenta (fungi); P. chrysosporium, Phanerochaete chrysosporium (fungi).

layer of *p*-TsOH/AHF-LNP aggregates and PVA molecular chains, and the presence of nanophase crazing due to the presence of these aggregates are the plausible mechanisms of the improved composite toughness. LNPs and *p*-TsOH also improved nanocomposite film UV blocking performance. The PVA/AHF-LNP composites are biodegradable and recyclable. These advantages suggest that PVA/AH-LNP nanocomposite can be an ideal bioplastic candidate for anti-ultraviolet packing application.

CRediT authorship contribution statement

Huihui Wang: conducted most of the experiments and drafted the manuscript. **Xiaoyan Tang:** conducted tensile tests. **Matthew A. Arvanitis:** conducted statistical analyses. **Vina Yang:** conducted

biodegradation tests. **Nicole Stark:** conducted permeability tests. **Chuanfu Liu:** reviewed manuscript and discussion on initiating the work. **John M. Considine:** designed tensile tests. **J.Y. Zhu:** initiated the research, conducted data analyses, made significant editing of the manuscript.

Declaration of Competing Interest

The authors report no declarations of interest.

Acknowledgements

This work was supported by the Guangzhou Elite Project of China, China Postdoctoral Science Foundation (2019TQ0102), and the USDA Forest Products Laboratory (FPL). Funding from these programs made the visiting appointment of Wang at FPL possible.

Appendix A. Supplementary data

Supplementary material related to this article can be found, in the online version, at doi:https://doi.org/10.1016/j.indcrop.2021.113584.

References

Adler, E., Wesslén, B., 1964. The behavior of lignin in alkaline pulping. Acta Chem. Scand. 18, 1311–1316.
Ago, M., Huan, S., Borghei, M., Raula, J., Kauppinen, E.I., Rojas, O.J., 2016. High-throughput synthesis of lignin particles (~30 nm to ~2 μm) via aerosol flow reactor: size fractionation and utilization in pickering emulsions. ACS Appl. Mater. Interfaces 8 (35), 23302–23310.
ASTM, 1998. Standard Test Method for Fungicides for Controlling Sapstain and Mold on Unseasoned Lumber (laboratory Method). ASTM Standard D4445-91, pp. 497–500, 11.01.
AWPA, 2014. AWPA Standard E10-12. AWPA Book of Standards, p. 656.
Bian, H., Chen, L., Gleisner, R., Dai, H., Zhu, J.Y., 2017. Producing wood-based nanomaterials by rapid fractionation of wood at 80 °C using a recyclable acid hydrotrope. Green Chem. 19, 3370–3379.
Cai, C., Hirth, K., Gleisner, R., Lou, H., Qiu, X., Zhu, J.Y., 2020. Maleic acid as a dicarboxylic acid hydrotrope for sustainable fractionation of wood at atmospheric pressure and ≤ 100 °C: mode and utility of lignin esterification. Green Chem. 22 (5), 1605–1617. https://doi.org/10.1039/C9GC04267A.
Chen, L., Dou, J., Ma, Q., Li, N., Wu, R., Bian, H., Yelle, D.J., Vuorinen, T., Fu, S., Pan, X., Zhu, J.Y., 2017. Rapid and near-complete dissolution of wood lignin at ≤ 80 °C by a recyclable acid hydrotrope. Sci. Adv. 3 (9), e1701735.
Cheng, G., Kent, M.S., He, L., Varanasi, P., Dibble, D., Arora, R., Deng, K., Hong, K., Melnichenko, Y.B., Simmons, B.A., Singh, S., 2012. Effect of ionic liquid treatment on the structures of lignins in solutions: molecular subunits released from lignin. Langmuir 28 (32), 11850–11857.
Cheng, J., Hirth, K., Ma, Q., Zhu, J., Wang, Z., Zhu, J.Y., 2019. Toward sustainable and complete wood valorization by fractionating lignin with low condensation using an acid hydrotrope at low temperatures (≤80 °C). Ind. Eng. Chem. Res. 58 (17), 7063–7073.
Chiellini, E., Cinelli, P., Ilieva, V.I., Ceccanti, A., Alexy, P., Bakos, D., 2003. Biodegradable hybrid polymer films based on poly(vinyl alcohol) and collagen hydrolyzate. Macromol. Symp. 197, 125–132.
Das, S., Paul, S., 2016. Mechanism of hydrotropic action of hydrotrope sodium cumene sulfonate on the solubility of di-t-butyl-methane: a molecular dynamics simulation study. J. Phy. Chem. B 120 (1), 173–183.
Del Río, J.C., Rencoret, J., Prinsen, P., Martínez, A.T., Ralph, J., Gutiérrez, A., 2012. Structural characterization of wheat straw lignin as revealed by analytical pyrolysis, 2D-NMR, and reductive cleavage methods. J. Agric. Food Chem. 60 (23), 5922–5935.
Farooq, M., Zou, T., Riviere, G., Sipponen, M.H., Osterberg, M., 2018. Strong, ductile, and waterproof cellulose nanofibril composite films with colloidal lignin particles. Biomacromolecules 20 (2), 693–704.
Frangville, C., Rutkevičius, M., Richter, A.P., Velev, O.D., Stoyanov, S.D., Paunov, V.N., 2012. Fabrication of environmentally biodegradable lignin nanoparticles. ChemPhysChem 13 (18), 4235–4243.
Ghosh, P., Han, G., De, M., Kim, C.K., Rotello, V.M., 2008. Gold nanoparticles in delivery applications. Adv. Drug Deliv. Rev. 60 (11), 1307–1315.
González-Vila, F.J., Almendros, G., del Rio, J.C., Martín, F., Gutiérrez, A., Romero, J., 1999. Ease of delignification assessment of wood from different Eucalyptus species by pyrolysis (TMAH)-GC/MS and CP/MAS 13C-NMR spectrometry. J. Anal. Appl. Pyrolysis 49 (1), 295–305.
Gross, R.A., Kalra, B., 2002. Biodegradable polymers for the environment. Science 297 (5582), 803–807.
Hiss, R., Hobeika, S., Lynn, C., Strobl, G., 1999. Network stretching, slip processes, and fragmentation of crystallites during uniaxial drawing of polyethylene and related copolymers. A comparative study. Macromolecules 32 (13), 4390–4403.
Kim, H., Ralph, J., 2010. Solution-state 2D NMR of ball-milled plant cell wall gels in DMSO-d6/pyridine-d5. Org. Biomol. Chem. 8 (3), 576–591.
Liang, J., Huang, Y., Zhang, L., Wang, Y., Ma, Y., Cuo, T., Chen, Y., 2009. Molecular-level dispersion of graphene into poly(vinyl alcohol) and effective reinforcement of their nanocomposites. Adv. Funct. Mater. 19 (14), 2297–2302.
Lievonen, M., Valle-Delgado, J.J., Mattinen, M.-L., Hult, E.-L., Lintinen, K., Kostiainen, M.A., Paananen, A., Szilvay, G.R., Setälä, H., Österberg, M., 2016. A simple process for lignin nanoparticle preparation. Green Chem. 18 (5), 1416–1422.
Lourenço, A., Gominho, J., Marques, A.V., Pereira, H., 2012. Reactivity of syringyl and guaiacyl lignin units and delignification kinetics in the kraft pulping of Eucalyptus globulus wood using Py-GC–MS/FID. Bioresour. Technol. 123, 296–302.
Lu, Q., Zhu, M., Zu, Y., Liu, W., Yang, L., Zhang, Y., Zhao, X., Zhang, X., Li, W., 2012. Comparative antioxidant activity of nanoscale lignin prepared by a supercritical antisolvent (SAS) process with non-nanoscale lignin. Food Chem. 135 (1), 63–67.
Lu, D., Zhou, J., Hou, S., Xiong, Q., Chen, Y., Pu, K., Ren, J., Duan, H., 2019. Functional macromolecule-enabled colloidal synthesis: from nanoparticle engineering to multifunctionality. Adv. Mater. 31 (44).
Luo, X., Morrin, A., Killard, A.J., Smyth, M.R., 2006. Application of nanoparticles in electrochemical sensors and biosensors. Electroanalysis 18 (4), 319–326.
Luo, X., Gleisner, R., Tian, S., Negron, J., Horn, E., Pan, X.J., Zhu, J.Y., 2010. Evaluation of mountain beetle infested lodgepole pine for cellulosic ethanol production by SPORL pretreatment. Ind. Eng. Chem. Res. 49 (17), 8258–8266.
Ma, Q., Chen, L., Wang, W., Yang, R., Zhu, J.Y., 2018. Direct production of lignin nanoparticles (LNPs) from wood using p-toluenesulfonic acid in an aqueous system at 80°C: characterization of LNP morphology, size, and surface charge. Holzforschung 72 (11), 933–942.
Mansfield, S.D., Kim, H., F.C, L., Ralph, J., 2012. Whole plant cell wall characterization using solution-state 2D NMR. Nat. Protoc. 7, 1579–1589. https://doi.org/10.1038/nprot.2012.064.
Morones, J.R., Elechiguerra, J.L., Camacho, A., Holt, K., Kouri, J.B., Ramírez, J.T., Yacaman, M.J., 2005. The bactericidal effect of silver nanoparticles. Nanotechnology 16 (10), 2346.
Myint, A.A., Lee, H.W., Seo, B., Son, W.S., Yoon, J., Yoon, T.J., Park, H.J., Yu, J., Lee, Y. W., 2016. One pot synthesis of environmentally friendly lignin nanoparticles with compressed liquid carbon dioxide as an antisolvent. Green Chem. 18 (7), 2129–2146.
Nair, S.S., Sharma, S., Pu, Y., Sun, Q., Pan, S., Zhu, J.Y., Deng, Y., Ragauskas, A.J., 2014. High shear homogenization of lignin to nanolignin and thermal stability of Nanolignin-Polyvinyl alcohol blends. ChemSusChem 7 (12), 3513–3520.
Popa, V.I., Căpraru, A.M., Grama, S., Măluţan, T., 2011. Nanoparticles based on modified lignins with biocide properties. Cell. Chem. Technol. 45 (3-4), 221–226.
Qian, Y., Deng, Y., Qiu, X., Li, H., Yang, D., 2014. Formation of uniform colloidal spheres from lignin, a renewable resource recovered from pulping spent liquor. Green Chem. 16 (4), 2156–2163.
Ragauskas, A.J., Beckham, G.T., Biddy, M.J., Chandra, R., Chen, F., Davis, M.F., Davison, B.H., Dixon, R.A., Gilna, P., Keller, M., 2014. Lignin valorization: improving lignin processing in the biorefinery. Science 344 (6185), 1246843.
Ren, X., 2003. Biodegradable plastics: a solution or a challenge? J. Clean. Prod. 11 (1), 27–40.
Richter, A.P., Bharti, B., Armstrong, H.B., Brown, J.S., Plemmons, D., Paunov, V.N., Stoyanov, S.D., Velev, O.D., 2016. Synthesis and characterization of biodegradable lignin nanoparticles with tunable surface properties. Langmuir 32 (25), 6468–6477.
Rinaldi, R., Jastrzebski, R., Clough, M.T., Ralph, J., Kennema, M., Bruijnincx, P.C.A., Weckhuysen, B.M., 2016. Paving the way for lignin valorisation: recent advances in bioengineering, biorefining and catalysis. Angewandte Chemie – Int. Edit. 55 (29), 8164–8215.
Salata, O.V., 2004. Applications of nanoparticles in biology and medicine. J. Nanobiotechnology 2 (1), 3.
Saxena, A., Ragauskas, A.J., 2009. Water transmission barrier properties of biodegradable films based on cellulosic whiskers and xylan. Carbohydr. Polym. 78 (2), 357–360.
Tian, D., Hu, J., Bao, J., Chandra, R.P., Saddler, J.N., Lu, C., 2017. Lignin valorization: lignin nanoparticles as high-value bio-additive for multifunctional nanocomposites. Biotechnol. Biofuels 10 (1), 192.
Wang, Y., Li, T., Ma, P., Bai, H., Xie, Y., Chen, M., Dong, W., 2016. Simultaneous enhancements of UV-shielding properties and photostability of poly (vinyl alcohol) via incorporation of sepia eumelanin. ACS Sustain. Chem. Eng. 4 (4), 2252–2258.
Wang, H., Chen, W., Zhang, X., Wei, Y., Zhang, A., Liu, S., Wang, X., Liu, C., 2018. Structural changes of bagasse dusring the homogeneous esterification with maleic anhydride in ionic liquid 1-allyl-3-methylimidazolium chloride. Polymers 10 (4), 433.
Wang, H., Hirth, K., Zhu, J., Ma, Q., Liu, C., Zhu, J.Y., 2019a. Dissolution of less-processed wood fibers without bleaching in an ionic liquid: effect of lignin condensation on wood component dissolution. Int. J. Biol. Macromol. 134, 740–748.
Wang, Z., Qiu, S., Hirth, K., Cheng, J., Wen, J., Li, N., Fang, Y., Pan, X., Zhu, J.Y., 2019b. Preserving both lignin and cellulose chemical structures: flow-through acid hydrotropic fractionation (AHF) at atmospheric pressure for complete wood valorization. ACS Sustain. Chem. Eng. 7, 10808–10820. https://doi.org/10.1021/acssuschemeng.9b01634.
Wen, J.-L., Sun, S.-L., Yuan, T.-Q., Sun, R.-C., 2015. Structural elucidation of whole lignin from Eucalyptus based on preswelling and enzymatic hydrolysis. Green Chem. 17 (3), 1589–1596.
Xiong, S., Wang, Y., Yu, J., Chen, L., Zhu, J., Hu, Z., 2014. Polydopamine particles for next-generation multifunctional biocomposites. J. Mater. Chem. A 2 (20), 7578–7587.

Yang, W., Owczarek, J.S., Fortunati, E., Kozanecki, M., Mazzaglia, A., Balestra, G.M., Kenny, J.M., Torre, L., Puglia, D., 2016. Antioxidant and antibacterial lignin nanoparticles in polyvinyl alcohol/chitosan films for active packaging. Ind. Crops Prod. 94, 800–811.

Zhang, X., Liu, W., Yang, D., Qiu, X., 2019. Biomimetic supertough and strong biodegradable polymeric materials with improved thermal properties and excellent UV-Blocking performance. Adv. Funct. Mater. 29 (4), 1806912.

Zhu, J.Y., Agarwal, U.P., Ciesielski, P.N., Himmel, M.E., Gao, R., Deng, Y., Morits, M., Österberg, M., 2021. Towards sustainable production and utilization of plant-biomass-based nanomaterials: a review and analysis of recent developments. Biotechnol. Biofuels 14. https://doi.org/10.1186/s130680021-01963-5.